THE JOURNAL OF PHYSICAL CHEMISTRY C

pubs.acs.org/JPCC Article

Contamination Mechanisms of Proton Exchange Membrane Fuel Cells - Mass Transfer Overpotential Origin

Keith Bethune, Jean St-Pierre,* Jacob M. LaManna, Daniel S. Hussey, and David L. Jacobson

Cite This: *J. Phys. Chem. C* 2020, 124, 24052−24065 Read Online

ABSTRACT: Several experimental methods were used to identify the cause of the concurrent increase in kinetic and mass transfer overpotentials during the contamination of proton exchange membrane fuel cells outfitted with a commercially relevant cathode catalyst loading of 0.1 mg Pt per cm^2. Neutron images demonstrated that the transport of liquid water through gas diffusion electrode materials was subtly affected by the presence of propene and methyl methacrylate in air at ppm levels (25 to 100 ppm propene, 12.5 to 50 ppm methyl methacrylate). Multioxidant polarization curves were obtained to isolate overpotentials (O_2, 21% O_2 + 79% He, and air). For all cases, neat air, 50 ppm propene in air, and 25 ppm methyl methacrylate in air, only kinetic and mass transfer overpotentials increased (O_2 reduction on a Pt supported on C catalyst, O_2 diffusion through the catalyst layer ionomer). Also, only the O_2 mass transfer coefficient associated with diffusion in the catalyst layer ionomer increased in the presence of 50 ppm propene and 25 ppm methyl methacrylate. Contaminant species adsorbed on the catalyst decrease the active surface area and increase both the real current density and the O_2 reduction kinetic overpotential. The smaller active surface area also brings the real current density closer to the limiting value, inducing an increase of the mass transfer overpotential connected with O_2 movement in the ionomer layer covering the catalyst. This mechanism was supported by a mathematical contamination model focused on contaminant and O_2 processes on the catalyst surface (adsorption, reaction, desorption).

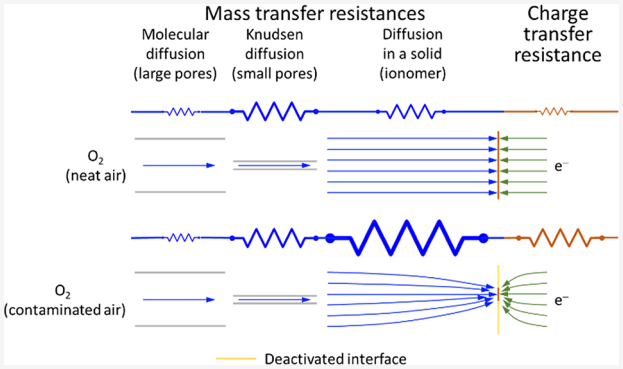

1. INTRODUCTION

Vehicles powered by proton exchange membrane fuel cells (PEMFCs) are currently commercialized in limited numbers. Degradation is still an issue delaying larger-scale adoption.[1] Contamination is an important source of degradation[2] increasing commercialization risks because system robustness partly relies on an air filter[3] that may be faulty or is no longer able to perform its function due to negligence about its maintenance. A multitude of contaminants exist, and the majority of those that have been tested have shown several detrimental effects[4] including kinetic, ohmic, and mass transfer overpotential increases.[5] The majority of the identified contaminants remain to be characterized preventing the development of contamination mechanisms that are important to devise effective mitigation strategies. Additionally, contamination mechanisms are generally species-specific due to, for example, the multitude of adsorbate configurations on the catalyst surface and chemical as well as electrochemical reactions[6] leaving many gaps in understanding including reactant mass transfer and water management.

Several broad classes of contaminants were identified: ions (cations and anions), inorganic, and organic species. The different cation effects on PEMFCs largely stem from their exchange with ionomer and membrane protons.[7−9] The presence of cations in the ionomer decreases the O_2 permeability because the water content is lessened by a smaller ion solvation[10] affecting hydrophilic ionomer channels, a gas transport path,[11] and corresponding limiting current. Furthermore, the drier ionomer decreases the real catalyst active surface by contraction, which brings the current density closer to the limiting value. Cations are also pushed toward the cathode during PEMFC operation due to the electric field, which locally decreases the proton concentration and the proton limiting current. Additionally, the O_2 reduction mechanism is perturbed by the local change in charge distribution,[12,13] which increases the H_2O_2 yield, lowers the electron transfer number, and increases the required O_2 flux (larger current density to limiting current density ratio). The

Received: July 7, 2020
Revised: October 4, 2020
Published: October 27, 2020

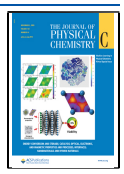

https://dx.doi.org/10.1021/acs.jpcc.0c06233
J. Phys. Chem. C 2020, 124, 24052−24065

Table 1. Selected Organic Contaminant Characteristics

species	acetonitrile	acetylene	bromomethane	isopropanol	methyl methacrylate	naphthalene	propene
dimensionless mass transfer resistance increase[30]	3.14	1.32	2.65	0.93	2.21	7.88	2.12
adsorption on C	yes[41]	yes[42]	yes[b,43]	yes[44]	yes[c,45]	yes[46]	yes[d,47]
solubility in H_2O ($mg \cdot L^{-1}$)	miscible[a]	1170	17,500	miscible	15,000	31.6	0.61
contaminant conversion (%)[48]	20 to 45 (0.55 to 0.65 V)	0.8 to 100 (0.55 to 0.85 V)	0 (0.1 to ~1 V)		49 to 57 (0.55 to 0.68 V)	detectable but not quantifiable (0.5 to 0.85 V)	43 to 89 (0.55 to 0.85 V)
dimensionless local current maximum loss and gain (%)[48]	−15 to 12	−17 to 18	−19 to 13	−9 to 5	−7 to 6	−25 to 14	−8 to 6
contamination timescale (h)[4]	1.6	3.13	19.6	2.33	0.55	0.41	0.25
recovery timescale (h)[4]	21.2	0.1	11.5	1.19	0.09	∞	0.04
cell voltage loss fraction that is recoverable[4]	0.97	1.02	0.22	1	1.03	0	1.06
fraction of contaminant scavenged[4]	0.064	8.6×10^{-5}	1.2×10^{-5}	0.075	0.0026	0.0030	1.1×10^{-5}

[a]786 $g \cdot L^{-1}$ for pure acetonitrile. [b]Dichloromethane. [c]Methyl acrylate. [d]4-Methyl-1-pentene.

higher H_2O_2 yield may also promote material degradation (C catalyst support, etc.), which may induce surface hydrophobicity and liquid water management (flooding) changes. Cation precursors (NH_3 hydrolysis leads to NH_4^+) and anions may adsorb on the Pt catalyst surface, which partially blocks the active area and increases the real current density closer to the limiting value. Salt precipitation is possible and preferentially occurs in flow channels and the gas diffusion layer under landings, occluding transport paths and modifying component hydrophobicity and water management. One or more of these effects were invoked to explain increases in mass transfer losses observed during Co^{2+} (from PtCo alloy catalyst dissolution),[14,15] NH_4^+ (reformate impurity),[16−18] Ca^{2+} (a component of roadside desalting agents, seawater component),[19−23] K^+ (seawater component),[21] Ba^{2+},[21] Al^{3+},[21] and Cl^- (seawater component)[24] contamination. Organic species adsorb on PEMFC C (gas diffusion layer, sublayer, catalyst support)[25] and Pt[26] materials, which, respectively, alter surface hydrophobicity and liquid water management, and increase the real current density by partially covering catalyst sites. These mechanisms were employed to explain mass transfer loss modifications resulting from contamination by toluene (solvent and industrial feedstock),[27,28] naphtha (potential fuel cell system component cleanser),[29] acetonitrile (butadiene production solvent),[30] acetylene (welding fuel and chemical manufacture precursor),[30] bromomethane (solvent and chemical manufacture precursor),[30] isopropanol (cleaning fluid and solvent),[30] methyl methacrylate (poly(methyl methacrylate) synthesis precursor),[30] naphthalene (mothball primary ingredient),[30] and propene (polypropylene synthesis precursor and petrochemical feedstock).[30] It is currently unclear if organic species predominantly affect mass transfer losses by adsorbing on C (water management change) or the Pt catalyst (increase in real current density). Clarification of this aspect would help focus on contamination mitigation activities because most air and system contaminants are organic.[31] Furthermore, the confirmation of an effect of organic contaminants on water management would suggest the existence of synergy between contaminants adsorbing on C and cationic contaminants, which require a liquid water path to reach the ionomer or membrane for ion exchange with protons.[7] From that standpoint, the understanding of contaminant mixtures, which are prevalent in the field,[32] would equally benefit from such a mechanism clarification.

In this report, several experimental methods were used to clarify the effects of two organic contaminants on O_2 mass transfer in PEMFCs. Neutron images were acquired to directly and locally quantify the amount of water in operating cells.[33−35] Polarization curves were completed with different oxidant compositions to obtain kinetic, ohmic, and mass transfer overpotentials.[36−38] Overall O_2 mass transfer coefficients were first derived from limiting current densities.[39] Subsequently, overall O_2 mass transfer coefficients were separated into elementary contributions by varying the oxidant diluent molecular mass and the O_2 concentration. This procedure extends a mass transfer coefficient separation method[39] and yields molecular and Knudsen diffusion and transport in the ionomer contributions. Overall mass transfer coefficients were finally used to validate an adapted contamination model. The unmodified model was derived for three different contaminant reaction kinetics on the catalyst surface: inactive species, active species with a slow rate-determining reaction, and active species with a slow rate-determining product desorption.[40]

2. EXPERIMENTAL SECTION

2.1. Contaminant Selection. Organic contaminants were first chosen from a previously established down selection list (Table 1)[4] because their effects are well documented and have shown increases in mass transfer resistance at sufficiently high contaminant concentrations with the exception of isopropanol (Table 1).[30] This list was subsequently reduced by using several criteria to minimize test duration, simplify test procedures, and facilitate result interpretation. Selection criteria included contaminant hydrophobicity, reactivity, current distribution uniformity, contamination and recovery timescales, the extent of the cell voltage loss that is recoverable, and the fraction of contaminant scavenged by liquid water drops.

Contaminant hydrophobicity is expected to affect liquid water management because contaminant adsorption on membrane/electrode assembly C materials (Table 1) modifies liquid water transport. A surrogate measure, the contaminant solubility in water (Table 1), was employed to evaluate contaminant hydrophobicity. A wide range of solubilities was observed, from sparsely soluble (propene) to miscible (acetonitrile, isopropanol).

https://dx.doi.org/10.1021/acs.jpcc.0c06233
J. Phys. Chem. C 2020, 124, 24052−24065

Most contaminants are not fully oxidized at a 0.55 V cell voltage (Table 1), which is in part supported by contaminant reduction and oxidation potentials.[49] This situation ensures that a supply of unaltered contaminant is available for adsorption. Tests completed with different contaminant concentrations and a momentary contaminant injection have demonstrated that the current distribution may be altered. The dimensionless change in current density is minimum for isopropanol, methyl methacrylate, and propene (Table 1). The absence of a contamination effect on the current density distribution simplifies data interpretation. Methyl methacrylate and propene exhibit fast contamination dynamics with contamination and recovery timescales resulting from a momentary contaminant exposure that are both shorter than an hour (Table 1 data taken from Table 3 in ref 4). Fast contamination dynamics are convenient because the scheduled neutron imaging beam time was limited. Additionally, most contaminants had a temporary effect with a cell voltage that eventually recovered after the contaminant injection was interrupted (Table 1 data were calculated using voltage changes taken from Table 3 in ref 4), which eliminated the need for a time-consuming rejuvenation procedure. For contaminants that dissolve in water, entrainment in product water drops is a possibility that leads to a decrease in contaminant concentration.[50] However, this scavenging effect is minimal for all contaminants listed in Table 1 (data taken from Table 2 in ref 4), which again facilitates data interpretation by limiting the number of contamination effects that need to be considered.

Propene and methyl methacrylate were selected because they covered a wide range of solubilities in water (respectively, 0.61 mg·L^{-1} and 15,000 mg·L^{-1}), were partially converted into oxidized products, minimally affected current distribution, had fast contamination kinetics, had a reversible effect on the cell voltage after contaminant injection was stopped, and were not significantly entrained by product water drops. These features minimize test duration, simplify test procedures, and facilitate result interpretation. Other reports detailing the effects of propene and methyl methacrylate on PEMFCs are available.[51−54]

2.2. Cells and MEAs. Two different Los Alamos National Laboratory single fuel cell designs were slightly adapted to access both in-plane (the neutron beam is perpendicular to the membrane/electrode assembly (MEA) plane) and through-plane (the neutron beam is parallel with the MEA plane) liquid water distributions. Both cells were described,[55,56] and only key features are mentioned. Only flow field designs were changed to conform with prior Hawaii Natural Energy Institute (HNEI) PEMFC contamination studies. All bipolar plates were made of Au-plated 6061 Al and had serpentine flow fields with 0.79 mm channel and 0.76 mm land widths. Cathode channels were 0.84 mm deep, whereas anode channels had a depth of 1.14 mm. The in-plane water distribution cell had an active surface area of 50 cm^2 (7.07 cm by 7.07 cm, anode/cathode, double/triple serpentine), whereas the through-plane water distribution cell had a surface area of 3.08 cm^2 (1.42 cm by 2.18 cm, anode/cathode, single/single serpentine).

Commercially relevant W. L. Gore and Associates[57] 5715 MEAs with 0.1 mg Pt cm^{-2} loadings on the anode and the cathode were employed. These catalyst coated membranes were inserted between SGL Carbon[57] SIGRACET 25 BC gas diffusion layers and polytetrafluoroethylene gaskets (anode/cathode, 152/203 μm thick (0.006/0.008 inches)). MEAs were conditioned using the following sequential protocol: 0.6 V for 1 h, cycling between 0.85 V for 5 min, and 0.6 V for 10 min for 20 cycles. The operating conditions for MEA conditioning were as follows: temperature (80 °C), cell inlet relative humidity (100%) and outlet pressure (48.7 kPag) for H_2 and air compartments, and, for the 50 cm^2 cell, flow rates of, respectively, 0.5 and 1.5 standard L·min^{-1} for H_2 and air.

2.3. Neutron Imaging. For the 50 cm^2 cell, tests were conducted with constant operating conditions and a temporary, stepwise injection of a contaminant in air. The cell was operated for a minimum of 1 h before and after the contaminant injection period, which lasted a minimum of 0.5 h for each concentration. Two contaminants and two reactant stream humidification schemes were explored (Table 2). The cathode reactant stream relative humidity was increased from 50 to 100% to maximize the amount of liquid water and accentuate the methyl methacrylate effect on liquid water management. Other operating parameters were maintained at a constant level: current density (1 A·cm^{-2}), temperature (80 °C), cell outlet pressure (48.7 kPag), and reactant stoichiometry (2) for H_2 and air compartments. The dry contaminant gas was preheated and injected downstream of the humidified air stream. During this process, the humidification of the resulting fuel cell inlet gas was kept constant by increasing the temperature setting of the humidifier unit.

Table 2. 50 cm^2 Cell Tests

contaminant	anode/cathode relative humidity (%)	contaminant concentration sequence (ppm)[a]
propene	100/50	0, 25, 50, 100, 0
methyl methacrylate	100/50	0, 12.5, 25, 50, 0
methyl methacrylate	100/100	0, 50, 0

[a]Dry gas basis.

For the 3.08 cm^2 cell, test conditions were adapted to mimic the local situation at both the inlet and outlet of the larger 50 cm^2 cell (differential operation). Anode and cathode gas flow rates were reduced by a factor of 2 and 3, respectively, because the 50 cm^2 cell had two anode flow field channels and three cathode flow field channels whereas the 3.08 cm^2 cell had a single flow field channel in both compartments. Channels for both cells have the same cross section (Section 2.2). The inlet pressures for the 50 cm^2 cell are 52/70 kPag for the anode/cathode, respectively (2 stoichiometry, 1 A·cm^{-2}). The inlet conditions of the larger cell were simulated by controlling the smaller cell inlet pressure, whereas for the outlet conditions of the 50 cm^2 cell, the 3.08 cm^2 cell outlet pressure was controlled. For the 3.08 cm^2 cell, the inlet conditions that were kept constant were as follows: current density (1 A·cm^{-2}), temperature (80 °C), absolute pressures of, respectively, 152 and 170 kPa for H_2 and air compartments, inlet relative humidities of, respectively, 100 and 50% for H_2 and air, and reactant stoichiometries of, respectively, 16.2 and 10.8 for H_2 and air streams. Outlet conditions for the 3.08 cm^2 cell were calculated using a General Motors model,[58,59] which yielded the following values: current density (0.875 A·cm^{-2}), temperature (80 °C), absolute pressure (48.7 kPag), inlet relative humidities of, respectively, 90 and 104% for H_2 and oxidant, reactant stoichiometries of 16.2 and 10.8 for H_2 and oxidant streams, respectively, and dry gas compositions of, respectively, 100% H_2 and 12.8% O_2 + 87.2% N_2 for the fuel and oxidant.

https://dx.doi.org/10.1021/acs.jpcc.0c06233
J. Phys. Chem. C 2020, 124, 24052−24065

As for Table 2 tests, during the contaminant injection period, the contaminant concentration was sequentially increased and each step lasted a minimum of 1 h. As for the steps before and after the contaminant injection period, their duration was unchanged and lasted a minimum of 1 h. Table 3 summarizes all tests.

Table 3. 3.08 cm^2 Cell Tests

contaminant	50 cm^2 cell region simulated by the operating conditions	contaminant concentration sequence (ppm)[a]
propene	inlet	0, 25, 0
propene	outlet	0, 25, 50, 0
methyl methacrylate	inlet	0, 12.5, 0
methyl methacrylate	outlet	0, 12.5, 25, 0
propene + methyl methacrylate	outlet	0, 12.5 (methyl methacrylate) + 25 (propene)

[a]Dry gas basis.

Neutron images were obtained at the National Institute of Standards and Technology, Neutron Imaging Facility (BT-2), Gaithersburg, MD.[60,61] Images were acquired during cell operation and for each step after a steady state was reached. Image data processing followed established procedures provided by the NIST and included (1) combining dark field, flat field, dry cell, and operating (wet) cell image sets using a 3 by 3 median spatial filter, (2) normalizing wet and dry images with the flat field image, (3) registering all combined images using the dry cell image as a reference, and (4) calculating the optical density (OD) with the flat-field normalized wet and dry images. Section 3.1 contains a discussion of the OD calculation.

Water content profiles were derived from neutron images by averaging across regions of interest in the optical density data. For the 50 cm^2 cell, the averaging domain for the vertical line scan profiles included the active area without flow redirection and port regions (Figure 1a), creating data that were dependent on the distance along the cell height and representing the inlet to outlet variability. For the 3.08 cm^2 cell, two averaging domains were considered (Figure 1b). Averaging domains for horizontal line scans were centered in the middle of the flow field landing and channel and covered 50% of their width. Averaging domains also extended beyond outer gas diffusion layer surfaces for a short distance into flow field channels and landings. Data were dependent on the distance along the MEA thickness. In Figure 1b, anode flow field channels are not visible because they contained an insufficient amount of liquid water.

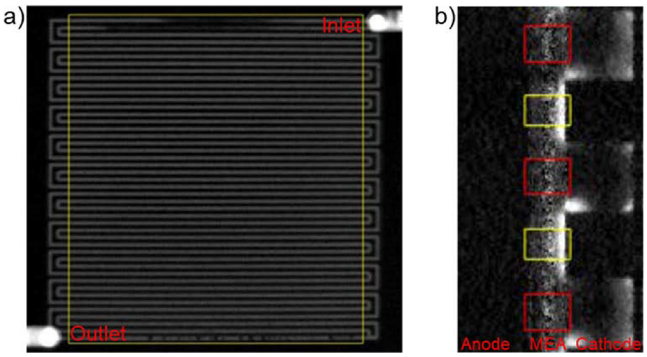

Figure 1. Averaging domains for the derivation of water content profiles. 50 (a) and 3.08 cm^2 (b) cells. Domains in panel (b) correspond to channels (red rectangles) and landings (yellow rectangles).

2.4. Polarization Curves. Polarization curves were acquired at HNEI using the 50 cm^2 cell and the following operating conditions that are consistent with Section 2.3 values with the exception of low current densities and the higher air relative humidity case of 100%: temperature (80 °C), outlet pressure (48.7 kPag) for H_2 and air compartments, inlet relative humidities of, respectively, 100 and 50% for H_2 and air, and reactant stoichiometry (2) for H_2 and air compartments with minimum gas flow rates set to values equivalent to a current density of 0.2 A·cm^{-2}. Polarization curves were obtained with three oxidants (100% O_2, 21% O_2 in N_2, and 21% O_2 in He) and three contaminant concentrations (no contaminant, 25 ppm methyl methacrylate, and 50 ppm propene on a dry gas basis). Current densities ranged from 0.1 to 1.5 A·cm^{-2} with 0.2 A·cm^{-2} steps between 0.2 and 1 A·cm^{-2} and 0.1 A·cm^{-2} steps above 1 A·cm^{-2}. The open circuit voltage was also recorded. Polarization curves were performed by first increasing the current density using a sequence of 1 min ramps and 1 min holds until the maximum current density was reached while maintaining the cell voltage above 0.2 V. Subsequently, the current density was decreased by steps lasting 3 min (the voltage during the last 15 s was averaged and recorded). For the contamination cases, a 10 min long step was used to average and record the cell voltage during the last 3 min of that step. The high frequency resistance (1 kHz) was recorded during tests using an Agilent[57] 4338B milliohmmeter.

Overpotentials were calculated using an established procedure.[38] The ohmic overpotential was obtained by multiplying the current density and the high frequency resistance values. The kinetic overpotential was derived by subtracting the cell voltage obtained with O_2 from the 1.23 V Nernst potential and adding the ohmic overpotential. The difference between cell voltages obtained with O_2 and the He mixture yields the sum of the concentration and ionomer phase mass transfer overpotentials. An extrapolation of this mixed overpotential to a 0 current density gives the concentration overpotential. Finally, the difference between cell voltages obtained with the He mixture and air leads to the gas-phase mass transfer overpotential.

2.5. O_2 Mass Transfer Coefficients. Tests designed to quantify and separate the O_2 mass transfer coefficient were carried out at HNEI. A constant cell voltage of 0.2 V was first applied to the 50 cm^2 cell for a period of 10 min to record the average limiting current density for each condition. Current values were averaged over the last 15 s and produced an evaluation of the average limiting current density i_{ave} (A·m^{-2}). Such tests were completed for five different oxidant flow rates. Data were subsequently fitted to the following equation to extract the overall O_2 mass transfer coefficient k (m·s^{-1})[39]

$$i_{ave} = i_e(1 - e^{-nFkp_r/RTi_e f}) \quad (1)$$

with i_e being the inlet reactant flow rate equivalent current density (A·m^{-2}), n being the number of electrons exchanged in the electrochemical reaction, F being the Faraday constant (96,500 C·mol^{-1}), p_r being the dry inlet reactant stream pressure (Pa), R being the ideal gas constant (8.3143 J·mol^{-1}·K^{-1}), T being the temperature (K), and f being the inert gas to

https://dx.doi.org/10.1021/acs.jpcc.0c06233
J. Phys. Chem. C 2020, 124, 24052−24065

reactant fraction in the dry inlet reactant stream. Equation 1 accounts for the uneven current density distribution occurring at relatively low stoichiometries. The overall mass transfer coefficient k is subsequently separated into molecular diffusion (k_m, m·s^{-1}), Knudsen diffusion (k_K, m·s^{-1}), and ionomer permeability (k_e, m·s^{-1}) contributions with changes in diluent molecular mass M (g·mol^{-1}) and O_2 concentration c (mol·m^{-3}).

$$\frac{1}{k} = \frac{1}{k_m(M)} + \frac{1}{k_{e+K}(c)} = \frac{1}{k_m(M)} + \frac{1}{k_e(c)} + \frac{1}{k_K} \quad (2)$$

The original separation method[39] was extended by taking advantage of the insensitivity of both molecular and Knudsen diffusion contributions to the O_2 concentration within a narrow concentration range. The existence of interfacial resistances is not explicitly accounted for in eq 2 as they are assumed to be negligible (infinitely thin interfaces). The importance of liquid water is also ignored because the O_2 concentration is ≥3 times lower than in air, which restrains the current density and amount of product liquid water in the electrodes.[62] A more detailed discussion of the method extension is available.[63] He, N_2, and CO_2 were used as diluents to create mixtures of 1, 3, 5, and 7% O_2. Tests were automated and followed a pre-established sequence that included changes in the diluent and flow rates. Tests were initiated with N_2 and were followed by He and CO_2 tests. For each diluent, tests included O_2 concentration and gas flow rates variations: 7% O_2 from high to low flow rates, 5% O_2 from low to high flow rates, 3% O_2 from high to low flow rates, and 1% O_2 from low to high flow rates. N_2 and He gas mixture flow rates were 1.044, 1.228, 1.445, 1.70, and 2.00 standard L·min^{-1}, whereas the CO_2 gas mixture flow rates were 0.9, 1.059, 1.246, 1.466, and 1.725 standard L·min^{-1}. The cell was operated for 1 h before each diluent sequence with an O_2 concentration of 7%. The test sequence was completed for three cases: no contaminant, 25 ppm methyl methacrylate, and 50 ppm propene. Other operating conditions were consistent with Sections 2.3 and 2.4 tests: temperature (80 °C), outlet pressure (48.7 kPag) for H_2 and air compartments, and inlet relative humidities of, respectively, 100 and 50% for H_2 and air.

3. RESULTS AND DISCUSSION

3.1. Neutron Images. A representative cell voltage transient is illustrated in Figure 2, which substantiates the existence of steady states during the acquisition of neutron images. Figure 2 also shows fast contamination dynamics with <15 min transition periods and a complete cell voltage recovery after methyl methacrylate injection. In the absence of a contaminant, steady-state cell voltages vary between 0.54 and 0.56 V for the 50 cm^2 cell and 0.58 and 0.64 V for the 3.08 cm^2 cell. The wider cell voltage range for the smaller cell is due to the significant changes in operating conditions (Section 2.3, Table 3). During contamination, steady-state cell voltages were consistent. For propene, cell voltages vary from 0.18 to 0.44 V for the 50 cm^2 cell and 0.2 to 0.46 V for the 3.08 cm^2 cell. For methyl methacrylate, cell voltages vary from 0.12 to 0.42 V for the 50 cm^2 cell and 0.13 to 0.44 V for the 3.08 cm^2 cell. The upper limit of these cell voltage ranges corresponding to the lowest contaminant concentrations, 0.46 V for propene and 0.44 V for methyl methacrylate, was sufficiently low to ensure that contaminants were not significantly oxidized. Table 1 indicates that conversion is below 43 and 49% at 0.55 V for propene and methyl methacrylate, respectively. Therefore, for the lower cell voltages of 0.46 and 0.44 V, contaminant conversion is expected to be even lower than at 0.55 V. Table 1 data were obtained with similar MEAs (ohmic resistance of approximately 0.056 Ω·cm^2 at 1 A·cm^{-2}),[49] which is comparable to an average of 0.064 Ω·cm^2 at 1 A·cm^{-2} for the present work (Section 3.2). The estimated cathode potentials from ref 48 and the present report data are similar because a hydrogen electrode was also used for both cases (anode potential of ∼0 V versus the RHE).

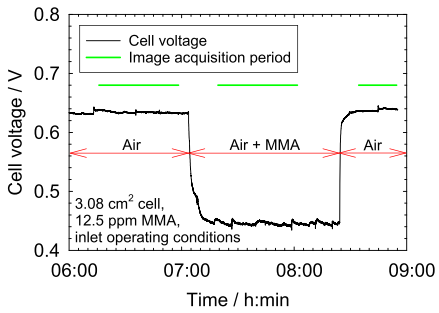

Figure 2. Exemplary cell voltage transient during a temporary injection of methyl methacrylate. Neutron images were acquired during steady-state voltage periods before, during, and after methyl methacrylate injection.

The color and intensity of Figure 3a,b images for the 50 cm^2 cell are related to the optical density OD scale (Figure 3c), which encompasses a 0 to 0.2 range and is representative of the water content[33]

$$\mathrm{OD} = \ln\left(\frac{I_{wet} - I_{dark}}{I_{dry} - I_{dark}}\right) \quad (3)$$

with I_{wet} being the neutron beam intensity during cell operation, I_{dry} being the reference neutron beam intensity obtained with a dry cell, and I_{dark} being the background neutron intensity (dark field). The absence of water during cell operation leads to an OD = 0, whereas for an OD = 1.3, saturation of the available space by water was observed in the outlet port. Figure 1a provides a context to interpret Figure 3a,b images. Figure 3a,b processed images only show liquid water over the cell active area, inlet and outlet ports, and tube fittings. The cell active area contains only a small amount of water (Figure 3a,b), which is barely perceivable against the dry inactive bipolar plate periphery and is located in the oxidant compartment close to the air outlet port even if the oxidant inlet stream is saturated. In comparison, Figures 1b, 4c,d, and 5c,d show even less water in the anode compartment. The averaged optical density over most of the active area (Figure 1a) is depicted in Figure 3c, which reveals a periodicity characteristic of the succession in landings and channels and the absence of significant differences between baseline and contamination cases with the exception of the cell center. The smaller optical density at this location for the contamination case only represents a small amount of water (maximum optical density of <0.02 against a 1.3 maximum), which is mainly attributed to a contamination effect.

Optical density data for the 3.08 cm^2 cell are illustrated in Figures 4 and 5 for propene and methyl methacrylate, respectively. Figure 1b and optical density scales displayed in Figures 4 and 5 offer a context to interpret neutron images. For inlet operating conditions (subsaturated oxidant stream),

https://dx.doi.org/10.1021/acs.jpcc.0c06233
J. Phys. Chem. C 2020, 124, 24052−24065

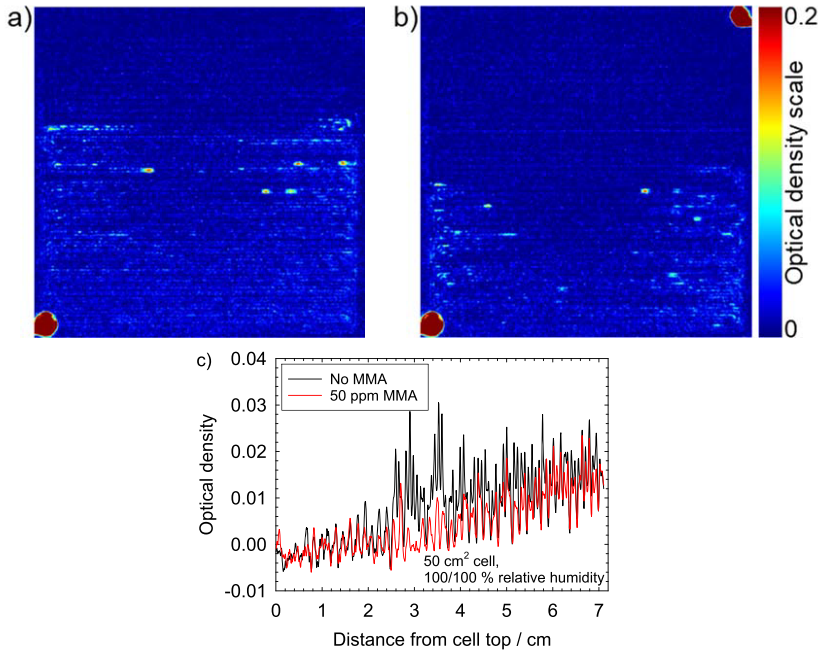

Figure 3. Neutron images for the 50 cm^2 active area cell before (a) and during (b) methyl methacrylate contamination. Optical density as a function of the distance along the cell height, from the inlet to the outlet (c). Operating conditions: 50 ppm methyl methacrylate, anode/cathode, 100/100% relative humidity.

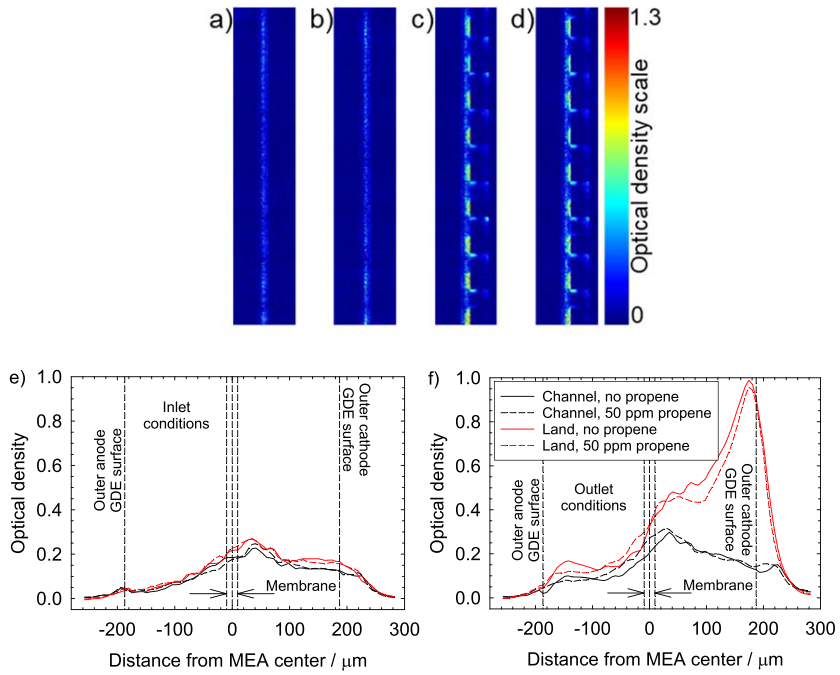

Figure 4. Neutron images for the 3.08 cm^2 active area cell before (a,c) and during (b,d) propene contamination for inlet (a,b) and outlet (c,d) operating conditions. 25 (b) and 50 ppm (d) propene. Optical density as a function of the distance through the membrane/electrode assembly plane for inlet (e) and outlet (f) operating conditions.

imperceptible amounts of water are observed in flow field channels (Figures 4a and 5a). In contrast, gas diffusion layers and the membrane are visible due to the substantial presence of water in gas diffusion layers and even more water in the membrane. Contaminants did not affect the water distribution for inlet operating conditions (Figures 4b and 5b). For wetter outlet operating conditions, water is additionally observed in cathode flow field channels and under landings (Figures 4c and 5c). The water distribution was again undisturbed by the presence of contaminants (Figures 4d and 5d). Optical density profiles for inlet (Figures 4e and 5e) and outlet (Figures 4f and 5f) operating conditions and channel and landing areas show the absence of significant contaminant effects. Only subtle changes are observed, most notably for the outlet operating conditions and under landings (Figures 4f and 5f). Figures 4 and 5 results, depicting marginally less water in the presence of contaminants, are consistent with Figure 3 data. The increase in optical density near MEA/land and channel interfaces in

https://dx.doi.org/10.1021/acs.jpcc.0c06233
J. Phys. Chem. C 2020, 124, 24052−24065

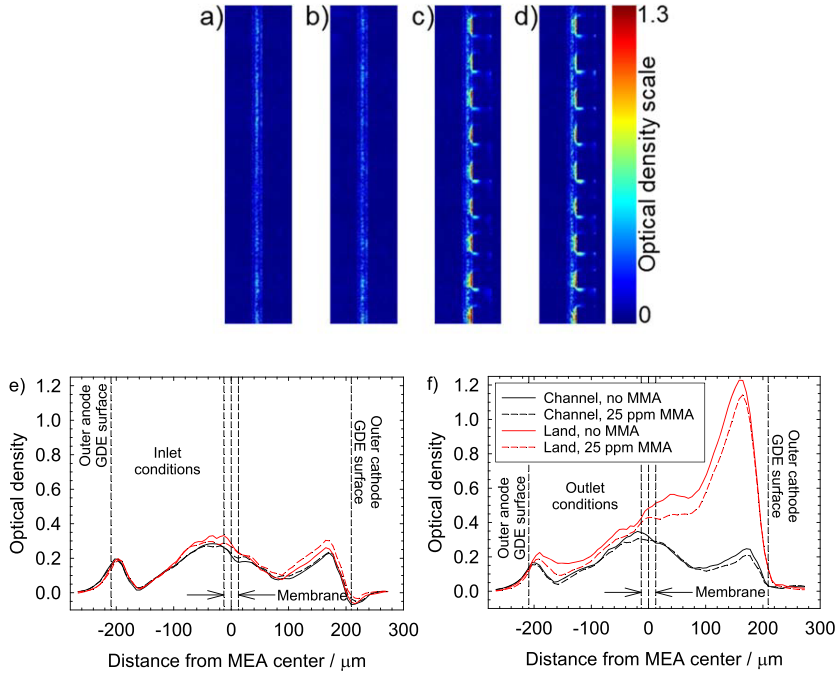

Figure 5. Neutron images for the 3.08 cm^2 active area cell before (a,c) and during (b,d) methyl methacrylate contamination for inlet (a,b) and outlet (c,d) operating conditions. 12.5 (b) and 25 ppm (d) methyl methacrylate. Optical density as a function of the distance through the membrane/electrode assembly plane for inlet (e) and outlet (f) operating conditions.

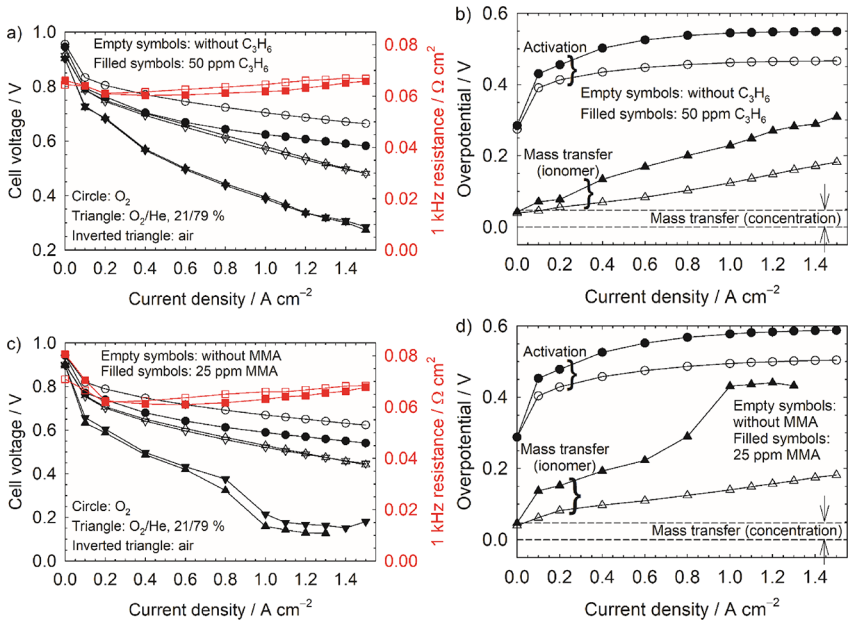

Figure 6. Polarization curves in the presence and absence of contamination and high frequency resistances obtained with O_2 for (a) propene and (c) methyl methacrylate cases. Overpotentials derived from polarization curves and high frequency resistances for (b) propene and (d) methyl methacrylate cases.

Figure 5e,f is ascribed to a small cell misalignment due to the repetitive use of the contaminant injection valve.

Liquid water management in gas diffusion electrodes is dependent on many structural and composition parameters including pore size distribution, tortuosity, material exposed (carbon, carbon surface groups, polytetrafluoroethylene), etc. It is surmised that the presence of the contaminant adsorbed on the carbon surface (Table 1) only significantly affects one of these parameters. This change is insufficient to modify to an appreciable extent liquid water management. Therefore, the source of the mass transfer loss induced by contamination must have another cause. Polarization curves were subsequently obtained using different oxidant compositions to isolate mass transfer overpotentials (concentration, gas phase, ionomer phase) and guide the search for a cause.

3.2. Polarization Curves. Polarization curves and high frequency resistances are depicted in Figure 6a,c. O_2 polarization curves were offset toward lower cell voltages in the presence of a contaminant, a clear sign of a larger kinetic overpotential. In contrast, the high frequency ohmic resistance

https://dx.doi.org/10.1021/acs.jpcc.0c06233
J. Phys. Chem. C 2020, 124, 24052−24065

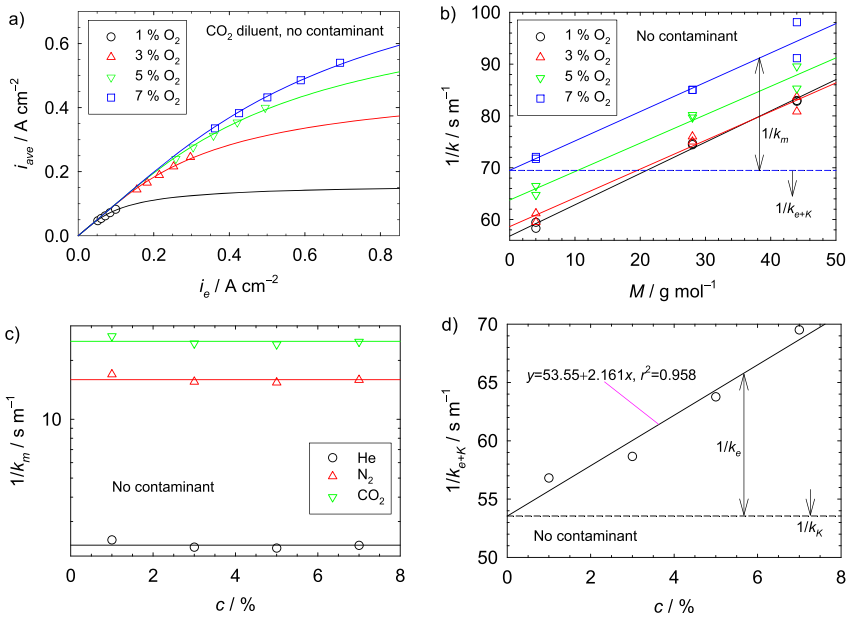

Figure 7. Plots of the average limiting current as a function of the inlet reactant flow rate equivalent current density for different O_2 concentrations (a). Overall O_2 mass transfer resistance as a function of the gas diluent molecular mass for different O_2 concentrations (b). Gas-phase molecular diffusion resistance as a function of the O_2 concentration for different gas diluent molecular masses (c). The lumped mass transfer resistance (gas-phase Knudsen diffusion, solid-phase ionomer permeability) as a function of the O_2 concentration (d).

(ohmic overpotential) and the difference between He mixture and air polarization curves (gas-phase mass transfer overpotential) were not affected by the presence of contaminants. Finally, the difference between O_2 and He mixture polarization curves (ionomer-phase mass transfer overpotential) increased in the presence of a contaminant. Only overpotentials that were significantly affected by contaminants are shown in Figure 6b,d. The calculated concentration mass transfer overpotential of 47 mV (first-order dependence on O_2 concentration for the exchange current density combined with a $2.303RT/F$ O_2 reduction Tafel slope leading to $(2.303RT/F)\log(1/0.21)$) is consistent with experimental values obtained by extrapolation.

The larger kinetic overpotential is consistent with contaminant adsorption on the Pt catalyst surface, which decreases the active surface area and increases the real current density. Concurrently, the smaller catalyst active area brings the real current density closer to the limiting value incurring a larger ionomer-phase mass transfer overpotential. It is hypothesized that the gas-phase mass transfer overpotential is not impacted because transport is easier than in a solid.

The larger methyl methacrylate kinetic and ionomer-phase mass transfer overpotentials are attributed to several factors that control adsorbate coverage and contaminant transport in the ionomer. However, the overall effect of all these parameters for propene and methyl methacrylate is not easily evaluated and compared due to knowledge gaps. For instance, to estimate the catalyst coverage, contaminant adsorption, reaction and desorption rate constants as a function of electrode potential are needed but are not available. Similarly, the permeability of contaminants through the catalyst layer ionomer is also missing. The constant ionomer-phase mass transfer overpotential for methyl methacrylate above 1 $A{\cdot}cm^{-2}$ (Figure 6d) is attributed to a low cathode potential that is insufficient for oxidation, which results in a maximum catalyst coverage.

Overpotentials clearly showed that the source of the mass transfer loss associated with contamination is located in the ionomer and is due to a decrease in the real catalyst active area. An additional confirmation was pursued by measuring and separating the O_2 mass transfer coefficient.

3.3. O_2 Mass Transfer Coefficients. The process for the measurement and the separation of the O_2 mass transfer coefficient is illustrated in Figure 7. First, the overall O_2 mass transfer coefficient is extracted from average current density versus inlet reactant flow rate equivalent current density plots by curve fitting to eq 1 (Figure 7a). This operation is repeated for each O_2 concentration and O_2 diluent in the absence of a contaminant. The second step consists of the separation of the gas-phase molecular diffusion contribution, which is accomplished by extrapolating the linear overall mass transfer resistance versus diluent molecular mass regressions to the origin, and yields the combined Knudsen diffusion and ionomer permeability resistance and the molecular diffusion resistance with the use of eq 2 (Figure 7b). The molecular diffusion resistance is constant within a narrow O_2 concentration range and is larger for higher diluent molecular masses (Figure 7c). For the last step, the combined Knudsen diffusion and ionomer permeability resistance is plotted as a function of the O_2 concentration. The linear regression leads to the Knudsen diffusion resistance at an O_2 concentration of 0 and the ionomer permeability resistance with the use of eq 2 (Figure 7d). O_2 mass transfer coefficients are summarized in Table 4.

Table 4. O_2 Mass Transfer Coefficients

contaminant	k_m ($m{\cdot}s^{-1}$)[a]	k_e ($m{\cdot}s^{-1}$)[b]	k_K ($m{\cdot}s^{-1}$)
none	0.0627	0.0220	0.0187
propene	0.0627[c]	0.00294	0.0187[c]
methyl methacrylate	0.0627[c]	0.00160	0.0187[c]

[a]For a N_2 diluent. [b]For 21% O_2. [c]Value assumed equal to the baseline case (no contaminant).

https://dx.doi.org/10.1021/acs.jpcc.0c06233
J. Phys. Chem. C 2020, 124, 24052−24065

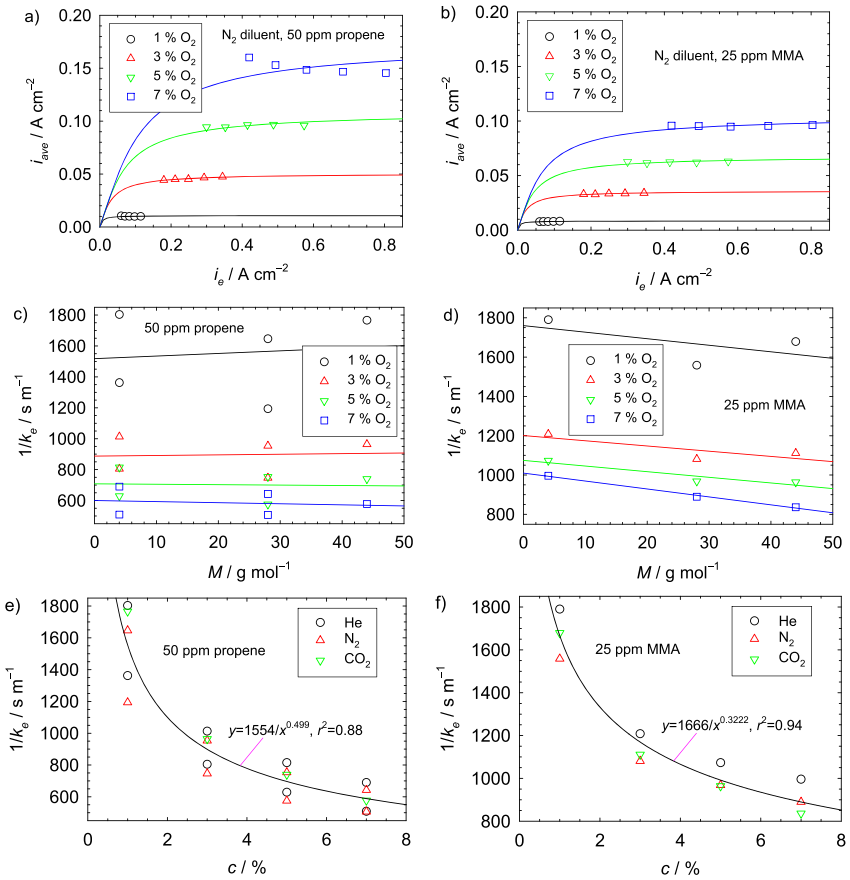

Figure 8. Plots of the average limiting current as a function of the inlet reactant flow rate equivalent current density for different O_2 concentrations and for 50 ppm propene (a) and 25 ppm methyl methacrylate (b). Ionomer permeability mass transfer resistance as a function of the gas diluent molecular mass for different O_2 concentrations and for 50 ppm propene (c) and 25 ppm methyl methacrylate (d). Ionomer permeability mass transfer resistance as a function of the O_2 concentration for different gas diluent molecular masses and for 50 ppm propene (e) and 25 ppm methyl methacrylate (f).

For both contamination cases, the first step for the measurement and the separation of the O_2 mass transfer coefficient remains the same (Figure 8a,b). Deviations between model and experimental data for cases involving a wide variation in gas flow rates (Figure 8a, 7% O_2) are attributed to changes in average gas pressure (pressure drop through the cell) and ionomer water content (subsaturated oxidant stream inlet). However, subsequent separation process steps were altered because the solid-phase ionomer permeability resistance is dominant. In the absence of contaminants, the overall O_2 mass transfer resistance is below 100 $s{\cdot}m^{-1}$ (Figure 7b) but exceeds 500 $s{\cdot}m^{-1}$ in the presence of propene and methyl methacrylate (data not shown). Figure 6b,d data indicated that the O_2 mass transfer overpotential for the gas phase (molecular diffusion) was not affected by contaminants. Knudsen diffusion is also not affected by contaminants as interactions between different molecules do not occur and pores contain slightly less liquid water on average (Figures 3c, 4e,f, and 5e,f). Therefore, the increase in overall O_2 mass transfer resistance in the presence of contaminants is solely due to the ionomer permeability contribution. Molecular and Knudsen diffusion mass transfer resistances in the absence of contamination (Table 4) were subtracted from the overall oxygen mass transfer resistance in the presence of contaminants to obtain the ionomer permeability mass transfer resistance (Figure 8c,d). This resistance is weakly dependent on the diluent molecular mass, which is ascribed to the relative O_2 and gas diluent permeability and molecular size.[64,65] Differences between Figure 8c,d are not due to the contaminants because their concentrations are too low to have a direct effect. Rather, differences stem from the larger effect of methyl methacrylate on mass transfer (larger molecule confined in narrow, hydrophilic ionomer channels) with a higher overpotential (Figure 6b,d) and ionomer permeability resistance (Figure 8c,d), which results in a smaller average current density and higher O_2 stoichiometry. Additional tests and analyses are needed for a more detailed explanation. Figure 8c,d data are replotted in Figure 8e,f to highlight the O_2 concentration dependency. The decrease in the ionomer permeability resistance with O_2 concentration is due to competitive adsorption for catalyst sites between the contaminant and O_2. O_2 more effectively competes at higher concentrations, which leads to a smaller catalyst coverage by contaminants and limits mass transfer issues (smaller real current density). Figure 8e,f data were empirically correlated to estimate the ionomer permeability mass transfer coefficient for a 21% O_2 concentration and complete Table 4.

Table 4 data demonstrate that the ionomer permeability mass transfer coefficient is smaller by approximately an order of magnitude in the presence of contaminants. Figure 8e,f suggests that this effect is linked to competitive adsorption between O_2 and contaminants on the catalyst surface. A generic contamination model was used to assess the link

https://dx.doi.org/10.1021/acs.jpcc.0c06233
J. Phys. Chem. C 2020, 124, 24052−24065

Table 5. Contamination Model Lumped Parameters

case	contaminant reaction rds[a]	contaminant product desorption rds
k_1 (mol·m^{-2}·s^{-1})	$\frac{k_{R,ads}k_{X,ads}c_Rc_X(p-p_s)^2}{k_{R,ads}c_R(p-p_s)+k_{R,des}+k_R} - k_{X,ads}c_X(p-p_s) - k_{X,des} - k_X$	$\frac{k_{R,ads}k_{X,ads}c_Rc_X(p-p_s)^2}{k_{R,ads}c_R(p-p_s)+k_{R,des}+k_R} - k_{X,ads}c_X(p-p_s) - k_{P_2,des}$
k_2 (mol·m^{-2}·s^{-1})	$k_{X,ads}c_X(p-p_s) - \frac{k_{R,ads}k_{X,ads}c_Rc_X(p-p_s)^2}{k_{R,ads}c_R(p-p_s)+k_{R,des}+k_R}$	$k_{X,ads}c_X(p-p_s) - \frac{k_{R,ads}k_{X,ads}c_Rc_X(p-p_s)^2}{k_{R,ads}c_R(p-p_s)+k_{R,des}+k_R}$
k_3	$\frac{k_{X,ads}c_X(p-p_s)}{k_{X,des}+k_X}$	$\frac{k_{X,ads}c_X(p-p_s)}{k_{P_2,des}}$
k_4	$\frac{k_{R,ads}(p-p_s)}{k_{R,\mathrm{des}}+k_R}$	$\frac{k_{R,ads}(p-p_s)}{k_{R,\mathrm{des}}+k_R}$

[a]For an unreactive contaminant (only adsorption and desorption take place), k_X is set to 0 in k_1 and k_3.

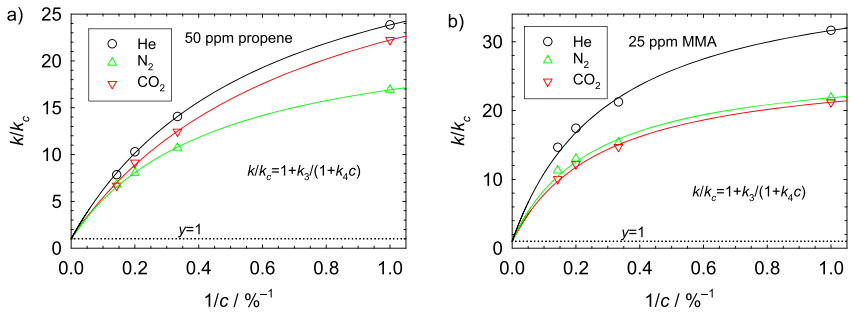

Figure 9. Experimental values of the overall O_2 mass transfer resistance in the presence of contaminants normalized by the overall O_2 mass transfer resistance in the absence of contaminants as a function of the inverse O_2 concentration for different gas diluent molecular masses. Air containing propene (a) and methyl methacrylate (b). Full lines represent a model fitted to each gas diluent data set (eq 8).

between contaminant adsorption and exacerbated mass transfer resistances.

3.4. Contamination Model. The contamination model includes adsorption, desorption, and reaction rate constants for both O_2 and contaminant.[40] These processes are included in mass balances for both species on the catalyst surface and lead at the steady state to an analytic solution relating a ratio of current densities to a ratio of two lumped parameters

$$\frac{i_c}{i} = 1 + \frac{k_2}{k_1} \tag{4}$$

with i_c being the current density in the presence of contaminants (A·m^{-2}), i being the current density in the absence of contaminants (A·m^{-2}), k_2 being a lumped parameter (mol·m^{-2}·s^{-1}), and k_1 being another lumped parameter (mol·m^{-2}·s^{-1}). Lumped parameters (Table 5) are O_2-concentration-dependent. The overall mass transfer coefficients were obtained under limiting current conditions (Section 2.5). The current density i_c in eq 4 is replaced by the O_2-concentration-dependent limiting current i_l (A·m^{-2}) expression[39]

$$i_l = i_c = nFk_cc \tag{5}$$

Equation 5 is valid in the presence of contaminants because the O_2 stoichiometry is high, varying from 2.6 to 17.2, and the current density is relatively uniform over the electrode active area. In contrast, the O_2 stoichiometry is low and less than 1.29 in the absence of contaminants. Under these conditions, the current density i in eq 4 is replaced by a simplified version of eq 1 because the exponential term argument is small (the exponential term is expanded, and only the first 2 terms are retained)

$$i_{\mathrm{ave}} = i = i_e(1 - e^{-nFkp_r/RTi_ef}) = i_e\left(1 - 1 + \frac{nFkp_r}{RTi_ef}\right) = \frac{nFkp_r}{RTf} = nFkc \tag{6}$$

The p_r/RTf term in eq 6 is the inlet O_2 concentration c for a dilute oxidant stream.[66] The combination of eqs 5 and 6 with eq 4 yields

$$\frac{i_c}{i} = \frac{nFk_cc}{nFkc} = \frac{k_c}{k} = 1 + \frac{k_2}{k_1} \tag{7}$$

The use of k_1 and k_2 expressions (Table 5) in eq 7 provides after rearrangement a relationship between the ratio of overall mass transfer coefficients in the absence and the presence of contaminants and the inlet O_2 concentration

$$\frac{k}{k_c} = 1 + \frac{k_3}{1 + k_4c} \tag{8}$$

Equation 8 parameters k_3 and k_4 are given in Table 5 and are independent of the O_2 concentration. Figure 9 illustrates comparisons between Section 3.3 experimental data and eq 8. The contamination model satisfactorily reproduces the effect of O_2 concentration for both contaminants and all gas diluents (all correlation coefficients exceed 0.997). This observation provides additional support to the correlation between contaminants adsorbed on the catalyst surface (competitive adsorption between O_2 and contaminants) and O_2 mass transfer. For high O_2 concentrations (low $1/c$ values), the contamination effect on O_2 mass transfer gradually decreases until it disappears with an infinite O_2 concentration ($k/k_c = 1$).

https://dx.doi.org/10.1021/acs.jpcc.0c06233
J. Phys. Chem. C 2020, 124, 24052−24065

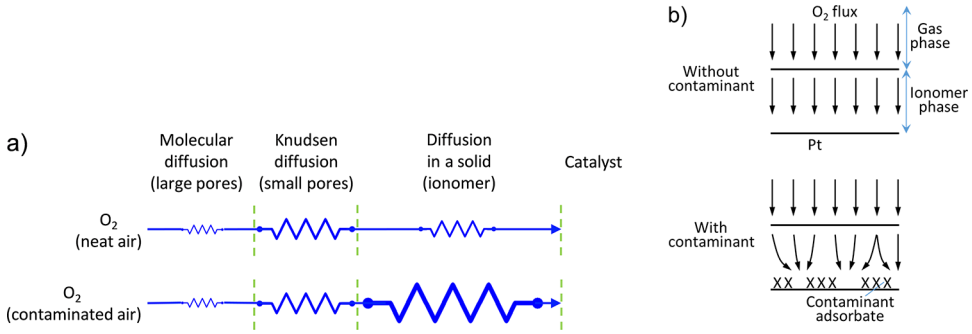

Figure 10. O_2 mass transfer path from the flow field channel to the catalyst surface and associated resistances (a). The relative importance of the different mass transfer processes for air is approximately indicated by the size of each resistance. Green dashed lines represent conceptual boundaries. O_2 mass transfer path adjacent to the catalyst (b).

As already stated in Section 3.3, the uneven effect of the gas diluent molecular mass will require additional analyses to determine its origin. The contamination mechanism rate-determining step (rds) cannot be ascertained because the model has the same form for each case (eq 8) although k_3 parameters are different (Table 5). Extrapolations of Figure 9 N_2 data to 21% O_2 result in k/k_c values of 3.19 for propene and 5.14 for methyl methacrylate. These values are consistent with Table 4 data, which lead to k/k_c values of 3.65 and 6.05 with the use of eq 2.

4. CONCLUSIONS

PEMFC operation in the presence of contaminants increases the O_2 reduction kinetic overpotential as well as the O_2 mass transfer overpotential. Neutron imaging eliminated the existence of major liquid water management modifications in the gas diffusion layer. Polarization curves obtained with different O_2 mixtures indicated an increase in O_2 mass transfer overpotential for the catalyst layer ionomer. This observation was supported by O_2 mass transfer coefficient measurements followed by separation into individual contributions and a contamination model, which includes competitive adsorption between O_2 and contaminant species on the catalyst surface. Figure 10a summarizes the relative size of each O_2 mass transfer resistance. Gas-phase molecular diffusion is the smallest resistance, whereas gas-phase Knudsen diffusion is the largest hindrance in the absence of contamination. In the presence of contaminants, the solid-phase diffusion resistance is exclusively affected and becomes the predominant impediment. The catalyst surface is partially covered by contaminant species (Figure 10b), which reduces the active surface and increases the real current density and O_2 reduction kinetic overpotential. The partially blocked catalyst surface locally disrupts mass transfer and forces O_2 to travel along a longer path with a progressively smaller cross section resulting in a higher mass transfer overpotential (the real current density is closer to the limiting current density). Figure 10b emphasizes the interconnection between both contamination effects.

It is expected that cation contaminants would have an even more pronounced effect on O_2 mass transfer because the O_2 permeability in ionomers is significantly diminished.[10,67−71] In contrast, the impact of organic contaminants on O_2 permeability in ionomers remains to be demonstrated and is expected because other ionomer properties are modified such as ionic conductivity.[72]

The contaminant effect on O_2 mass transfer in PEMFCs is similar to the effect of catalyst loading.[73−75] For both cases, the decrease in catalyst active surface area promotes an increase in O_2 mass transfer overpotential. For a catalyst loading change, the remaining active area is invariant with the same Pt atoms exposed to the oxidant. However, for the contamination case at the steady state, the localization of the smaller catalyst area fluctuates over time because contaminant species continuously adsorb, react, and desorb. The available catalyst area remains constant, but the position of free sites dynamically varies. It is conceivable to control in situ the catalyst loading by identifying a contaminant that reversibly blocks catalyst sites without affecting the O_2 reduction mechanism (Tafel slope, H_2O_2 yield, etc.). This approach is desirable to more directly compare data by minimizing the variability in catalyst composition and structure inherent to manufacturing operations.

■ AUTHOR INFORMATION

Corresponding Author

Jean St-Pierre − *Hawaii Natural Energy Institute, University of Hawaii - Manoa, Honolulu, Hawaii 96822, United States*; Phone: 1-808-956-3909; Email: jsp7@hawaii.edu

Authors

Keith Bethune − *Hawaii Natural Energy Institute, University of Hawaii - Manoa, Honolulu, Hawaii 96822, United States*

Jacob M. LaManna − *Physical Measurement Laboratory, National Institute of Standards and Technology, Gaithersburg, Maryland 20874, United States*

Daniel S. Hussey − *Physical Measurement Laboratory, National Institute of Standards and Technology, Gaithersburg, Maryland 20874, United States*; orcid.org/0000-0002-2851-4367

David L. Jacobson − *Physical Measurement Laboratory, National Institute of Standards and Technology, Gaithersburg, Maryland 20874, United States*

Complete contact information is available at: https://pubs.acs.org/10.1021/acs.jpcc.0c06233

Author Contributions

K.B. completed all equipment transfers between the NIST and HNEI, experimental measurements, and neutron image processing. J.St-P. conceived the project, completed polarization curves and mass transfer coefficient analyses, adapted the contamination model, and wrote the article draft. All authors reviewed the article draft and provided comments that were subsequently integrated into the revised text. J.M.LaM. facilitated the experiment at the NIST and trained K.B. and J.St-P. on neutron image processing. D.S.H. and D.L.J.

https://dx.doi.org/10.1021/acs.jpcc.0c06233
J. Phys. Chem. C 2020, 124, 24052−24065

developed the neutron imaging processing tools and data acquisition.

Notes

The authors declare no competing financial interest.

■ ACKNOWLEDGMENTS

Authors are grateful to the National Institute of Standards and Technology for the use of their Center for Neutron Research facilities, the Los Alamos National Laboratory and the Fuel Cell Performance and Durability (FC-PAD) consortium for information and the use of the neutron imaging fuel cell hardware, the Office of Naval Research for award N00014-16-1-2116, and Hawaiian Electric for supporting the Hawaii Sustainable Energy Research Facility operations.

■ REFERENCES

(1) Wang, G.; Yu, Y.; Liu, H.; Gong, C.; Wen, S.; Wang, X.; Tu, Z. Progress on Design and Development of Polymer Electrolyte Membrane Fuel Cell Systems for Vehicle Applications: A Review. *Fuel Process. Technol.* **2018**, *179*, 203−228.

(2) Büchi, F. N.; Inaba, M.; Schmidt, T. J. *Polymer Electrolyte Fuel Cell Durability*; Springer: 2009, pp. 289−321, DOI: 10.1007/978-0-387-85536-3.

(3) Higgins, S. R.; Ewan, J.; St-Pierre, J.; Severa, G.; Davies, K.; Bethune, K.; Goodarzi, A.; Rocheleau, R. Environmental Sensor System for Expanded Capability of PEM Fuel Cell Use in High Air Contaminant Conditions. *Int. J. Hydrogen Energy* **2018**, *43*, 22584−22594.

(4) St-Pierre, J.; Zhai, Y.; Angelo, M. S. Effect of Selected Airborne Contaminants on PEMFC Performance. *J. Electrochem. Soc.* **2014**, *161*, F280−F290.

(5) St-Pierre, J.; Wilkinson, D. P.; Knights, S.; Bos, M. Relationships between Water Management, Contamination and Lifetime Degradation in PEFC. *J. New Mater. Electrochem. Syst.* **2000**, *3*, 99−106.

(6) Zhai, Y.; St-Pierre, J. Acetylene Contamination Mechanisms in the Cathode of Proton Exchange Membrane Fuel Cells. *ChemElectroChem* **2017**, *4*, 655−670.

(7) St-Pierre, J. PEMFC Contamination Model: Foreign Cation Exchange with Ionomer Protons. *J. Power Sources* **2011**, *196*, 6274−6283.

(8) Weber, A. Z.; Delacourt, C. Mathematical Modelling of Cation Contamination in a Proton-Exchange Membrane. *Fuel Cells* **2008**, *8*, 459−465.

(9) Kienitz, B. L.; Baskaran, H.; Zawodzinski, T. A., Jr. Modeling the Steady-State Effects of Cationic Contamination on Polymer Electrolyte Membranes. *Electrochim. Acta* **2009**, *54*, 1671−1679.

(10) Okada, T.; Dale, J.; Ayato, Y.; Asbjørnsen, O. A.; Yuasa, M.; Sekine, I. Unprecedented Effect of Impurity Cations on the Oxygen Reduction Kinetics at Platinum Electrodes Covered with Perfluorinated Ionomer. *Langmuir* **1999**, *15*, 8490−8496.

(11) Broka, K.; Ekdunge, P. Oxygen and Hydrogen Permeation Properties and Water Uptake of Nafion® 117 Membrane and Recast Film for PEM Fuel Cell. *J. Appl. Electrochem.* **1997**, *27*, 117−123.

(12) Durst, J.; Chatenet, M.; Maillard, F. Impact of Metal Cations on the Electrocatalytic Properties of Pt/C Nanoparticles at Multiple Phase Interfaces. *Phys. Chem. Chem. Phys.* **2012**, *14*, 13000−13009.

(13) Strmcnik, D.; Li, D.; Lopes, P. P.; Tripkovic, D.; Kodama, K.; Stamenkovic, V. R.; Markovic, N. M. When Small is Big: The Role of Impurities in Electrocatalysis. *Top. Catal.* **2015**, *58*, 1174−1180.

(14) Li, H.; Gazzarri, J.; Tsay, K.; Wu, S.; Wang, H.; Zhang, J.; Wessel, S.; Abouatallah, R.; Joos, N.; Schrooten, J. PEM Fuel Cell Cathode Contamination in the Presence of Cobalt Ion (Co^{2+}). *Electrochim. Acta* **2010**, *55*, 5823−5830.

(15) Oezaslan, M.; Hasché, F.; Strasser, P. Oxygen Electroreduction on $PtCo_3$, PtCo and Pt_3Co Alloy Nanoparticles for Alkaline and Acidic PEM Fuel Cells. *J. Electrochem. Soc.* **2012**, *159*, B394−B405.

(16) Yuan, X.-Z.; Li, H.; Yu, Y.; Jiang, M.; Qian, W.; Zhang, S.; Wang, H.; Wessel, S.; Cheng, T. T. H. Diagnosis of Contamination Introduced by Ammonia at the Cathode in a Polymer Electrolyte Membrane Fuel Cell. *Int. J. Hydrogen Energy* **2012**, *37*, 12464−12473.

(17) Lopes, T.; Sansiñena, J.-M.; Mukundan, R.; Hussey, D. S.; Jacobson, D. L.; Garzon, F. H. Diagnosing the Effects of Ammonia Exposure on PEFC Cathodes. *J. Electrochem. Soc.* **2014**, *161*, F703−F709.

(18) Gomez, Y. A.; Oyarce, A.; Lindbergh, G.; Lagergren, C. Ammonia Contamination of a Proton Exchange Membrane Fuel Cell. *J. Electrochem. Soc.* **2018**, *165*, F189−F197.

(19) Wang, X.; Qi, J.; Ozdemir, O.; Uddin, A.; Pasaogullari, U.; Bonville, L. J.; Molter, T. Ca^{2+} as an Air Impurity in Polymer Electrolyte Membrane Fuel Cells. *J. Electrochem. Soc.* **2014**, *161*, F1006−F1014.

(20) Uddin, M. A.; Wang, X.; Park, J.; Pasaogullari, U.; Bonville, L. Distributed Effects of Calcium Ion Contaminant on Polymer Electrolyte Fuel Cell Performance. *J. Power Sources* **2015**, *296*, 64−69.

(21) Qi, J.; Wang, X.; Ozdemir, M. O.; Uddin, M. A.; Bonville, L.; Pasaogullari, U.; Molter, T. Effect of Cationic Contaminants on Polymer Electrolyte Fuel Cell Performance. *J. Power Sources* **2015**, *286*, 18−24.

(22) Park, J.; Uddin, M. A.; Pasaogullari, U.; Bonville, L. Changes in the Wettability of Polymer Electrolyte Fuel Cells Components during Cationic Contamination and Mitigation. *Int. J. Hydrogen Energy* **2017**, *42*, 21146−21157.

(23) Banas, C. J.; Bonville, L.; Pasaogullari, U. Linking Foreign Cationic Contamination of PEM Fuel Cells to the Local Water Distribution. *J. Electrochem. Soc.* **2017**, *164*, F1100−F1109.

(24) Li, H.; Zhang, S.; Qian, W.; Yu, Y.; Yuan, X.-Z.; Wang, H.; Jiang, M.; Wessel, S.; Cheng, T. T. H. Impacts of Operating Conditions on the Effects of Chloride Contamination on PEM Fuel Cell Performance and Durability. *J. Power Sources* **2012**, *218*, 375−382.

(25) Zhang, X.; Gao, B.; Creamer, A. E.; Cao, C.; Li, Y. Adsorption of VOCs onto Engineered Carbon Materials: A Review. *J. Hazard. Mater.* **2017**, *338*, 102−123.

(26) Itagaki, Y.; Mori, M.; Sadaoka, Y. EMF Response of the YSZ Based Potentiometric Sensors in VOC Contaminated Air. *Curr. Opin. Electrochem.* **2018**, *11*, 72−77.

(27) Li, H.; Zhang, J.; Fatih, K.; Wang, Z.; Tang, T.; Shi, Z.; Wu, S.; Song, D.; Zhang, J.; Jia, N.; et al. Polymer Electrolyte Membrane Fuel Cell Contamination: Testing and Diagnosis of Toluene-Induced Cathode Degradation. *J. Power Sources* **2008**, *185*, 272−279.

(28) Li, H.; Zhang, J.; Shi, Z.; Song, D.; Fatih, K.; Wu, S.; Wang, H.; Zhang, J.; Jia, N.; Wessel, S.; et al. PEM Fuel Cell Contamination: Effects of Operating Conditions on Toluene-Induced Cathode Degradation. *J. Electrochem. Soc.* **2009**, *156*, B252−B257.

(29) Ozdemir, M. O.; Uddin, M. A.; Ganesan, S.; Pasaogullari, U.; Collins, W. P.; Bonville, L.; Molter, T. Experimental Observation of the Effect of Cleansing Agents on the Performance of Polymer Electrolyte Fuel Cells. *Int. J. Hydrogen Energy* **2017**, *42*, 26068−26083.

(30) St-Pierre, J.; Ge, J.; Zhai, Y.; Reshetenko, T. V.; Angelo, M. PEMFC Cathode Contamination Mechanisms for Several VOCs - Acetonitrile, Acetylene, Bromomethane, Iso-Propanol, Methyl Methacrylate, Naphthalene and Propene. *ECS Trans.* **2013**, *58*, 519−528.

(31) St-Pierre, J.; Angelo, M.; Bethune, K.; Ge, J.; Higgins, S.; Reshetenko, T. V.; Virji, M. B. V.; Zhai, Y. PEMFC Contamination - Fundamentals and Outlook. *ECS Trans.* **2014**, *61*, 1−14.

(32) Qi, J.; Zhai, Y.; St-Pierre, J. Effect of Contaminant Mixtures in Air on Proton Exchange Membrane Fuel Cell Performance. *J. Power Sources* **2019**, *413*, 86−97.

(33) Satija, R.; Jacobson, D. L.; Arif, M.; Werner, S. A. In Situ Neutron Imaging Technique for Evaluation of Water Management Systems in Operating PEM Fuel Cells. *J. Power Sources* **2004**, *129*, 238−245.

(34) Mukundan, R.; Borup, R. L. Visualising Liquid Water in PEM Fuel Cells Using Neutron Imaging. *Fuel Cells* **2009**, *9*, 499−505.

(35) Boillat, P.; Lehmann, E. H.; Trtik, P.; Cochet, M. Neutron Imaging of Fuel Cells - Recent Trends and Future Prospects. *Curr. Opin. Electrochem.* **2017**, *5*, 3−10.
(36) Rho, Y. W.; Velev, O. A.; Srinivasan, S.; Kho, Y. T. Mass Transport Phenomena in Proton Exchange Membrane Fuel Cells Using O_2/He, O_2/Ar, and O_2/N_2 Mixtures: I. Experimental Analysis. *J. Electrochem. Soc.* **1994**, *141*, 2084−2089.
(37) Rho, Y. W.; Srinivasan, S.; Kho, Y. T. Mass Transport Phenomena in Proton Exchange Membrane Fuel Cells Using O_2/He, O_2/Ar, and O_2/N_2 Mixtures: II. Theoretical Analysis. *J. Electrochem. Soc.* **1994**, *141*, 2089−2096.
(38) Breitkopf, C., Swider-Lyons, K. *Springer Handbook of Electrochemical Energy*; Springer: 2017, pp. 611−647.
(39) Reshetenko, T. V.; St-Pierre, J. Separation Method for Oxygen Mass Transport Coefficient in Gas and Ionomer Phases in PEMFC GDE. *J. Electrochem. Soc.* **2014**, *161*, F1089−F1100.
(40) St-Pierre, J. PEMFC Contamination Model: Competitive Adsorption Followed by an Electrochemical Reaction. *J. Electrochem. Soc.* **2009**, *156*, B291−B300.
(41) Park, J. J.; Jung, S. Y.; Park, C. G.; Lee, S. C.; Kim, J. N.; Kim, J. C. The removal of the Acetonitrile Using Activated Carbon-Based Sorbent Impregnated with Sodium Carbonate. *Korean J. Chem. Eng.* **2012**, *29*, 489−493.
(42) Onyestyák, G.; Valyon, J.; Hernádi, K.; Kiricsi, I.; Rees, L. V. C. Equilibrium and Dynamics of Acetylene Sorption in Multiwalled Carbon Nanotubes. *Carbon* **2003**, *41*, 1241−1248.
(43) Eissmann, R. N.; Le Van, M. D. Coadsorption of Organic Compounds and Water Vapor on BPL Activated Carbon. 2. 1,1,2-Trichloro-1,2,2-Trifluoroethane and Dichloromethane. *Ind. Eng. Chem. Res.* **1993**, *32*, 2752−2757.
(44) Reddy, P. M. K.; Krushnamurty, K.; Subrahmanyam, C. Surface Modification of Carbon Fabric for Isopropanol Removal from Gas Stream. *Microelectron. Eng.* **2014**, *126*, 60−64.
(45) Wang, F.; Li, J.; Wang, J.; Gao, H. Adsorption of Acrylonitrile and Methyl Acrylate on Activated Carbon in a Packed Bed Column. *Adsorption* **2006**, *12*, 205−212.
(46) Di Gregorio, F.; Parrillo, F.; Salzano, E.; Cammarota, F.; Arena, U. Removal of Naphthalene by Activated Carbons from Hot Gas. *Chem. Eng. J.* **2016**, *291*, 244−253.
(47) Lai, M.-H.; Shih, Y.-L.; Chen, Y.-H.; Shu, S.-H.; Chung, T.-W. Equilibrium Isotherms of the Adsorption of Pyrolysis Gases from Polymer Products. *J. Chem. Eng. Data* **2010**, *55*, 723−727.
(48) St-Pierre, J.; Zhai, Y.; Ge, J.; Reshetenko, T.; Angelo, M.; Molter, T.; Bonville, L.; Pasaogullari, U.; Wang, X.; Qi, J.; et al. *DOE Hydrogen and Fuel Cells Program - 2014 Annual Progress Report*; United States Department of Energy: 2014.
(49) St-Pierre, J.; Zhai, Y.; Ge, J. Relationships between PEMFC Cathode Kinetic Losses and Contaminants' Dipole Moment and Adsorption Energy on Pt. *J. Electrochem. Soc.* **2016**, *163*, F247−F254.
(50) St-Pierre, J.; Wetton, B.; Zhai, Y.; Ge, J. Liquid Water Scavenging of PEMFC Contaminants. *J. Electrochem. Soc.* **2014**, *161*, E3357−E3364.
(51) Ge, J.; St-Pierre, J.; Zhai, Y. PEMFC Cathode Catalyst Contamination Evaluation with a RRDE - Propene and Naphthalene. *Electrochim. Acta* **2014**, *138*, 437−446.
(52) Ge, J.; St-Pierre, J.; Zhai, Y. PEMFC Cathode Catalyst Contamination Evaluation with a RRDE-Methyl Methacrylate. *Int. J. Hydrogen Energy* **2014**, *39*, 18351−18361.
(53) St-Pierre, J.; Virji, M. B. V. Cell Performance Distribution in a Low-Temperature Proton Exchange Membrane Fuel Cell Stack during Propene Contamination. *J. Appl. Electrochem.* **2016**, *46*, 169−181.
(54) Reshetenko, T. V.; St-Pierre, J. Effects of Propylene, Methyl Methacrylate and Isopropanol Poisoning on Spatial Performance of a Proton Exchange Membrane Fuel Cell. *J. Power Sources* **2018**, *378*, 216−224.
(55) Mukundan, R.; Davey, J. R.; Rockward, T.; Spendelow, J. S.; Pivovar, B.; Hussey, D. S.; Jacobson, D. L.; Arif, M.; Borup, R. Imaging of Water Profiles in PEM Fuel Cells Using Neutron Radiography: Effect of Operating Conditions and GDL Composition. *ECS Trans.* **2007**, *11*, 411−422.
(56) Mukundan, R.; Davey, J.; Lujan, R.; Spendelow, J.; Kim, Y. S.; Hussey, D. S.; Jacobson, D.; Arif, M.; Borup, R. L. Performance and Durability of PEM Fuel Cells Operated at Sub-Freezing Temperatures. *ECS Trans.* **2008**, *16*, 1939−1950.
(57) Certain trade names and company products are mentioned in the text or identified in an illustration in order to adequately specify the experimental procedure and equipment used. In no case does such identification imply recommendation or endorsement by the National Institute of Standards and Technology, nor does it imply that the products are necessarily the best available for the purpose.
(58) Vielstich, W., Yokokawa, H., Gasteiger, H. A. *Handbook of Fuel Cells: Fundamentals, Technology and Applications*; John Wiley & Sons: 2009, Vol. 6, Chap. *43*, pp. 631−657.
(59) Weber, A. Z.; Borup, R. L.; Darling, R. M.; Das, P. K.; Dursch, T. J.; Gu, W.; Harvey, D.; Kusoglu, A.; Litster, S.; Mench, M. M.; et al. A Critical Review of Modeling Transport Phenomena in Polymer-Electrolyte Fuel Cells. *J. Electrochem. Soc.* **2014**, *161*, F1254−F1299.
(60) Hussey, D. S.; Jacobson, D. L.; Arif, M.; Coakley, K. J.; Vecchia, D. F. In Situ Fuel Cell Water Metrology at the NIST Neutron Imaging Facility. *J. Fuel Cell Sci. Technol.* **2010**, *7*, No. 021024.
(61) Hussey, D. S.; Spernjak, D.; Weber, A. Z.; Mukundan, R.; Fairweather, J.; Brosha, E. L.; Davey, J.; Spendelow, J. S.; Jacobson, D. L.; Borup, R. L. Accurate Measurement of the through-Plane Water Content of Proton-Exchange Membranes Using Neutron Radiography. *J. Appl. Phys.* **2012**, *112*, 104906.
(62) Jacobson, D. L.; Hussey, D. S.; Baltic, E. M.; Arif, M. Neutron Imaging Study of the Water Transport in Operating Fuel Cells. In *2016 DOE Annual Merit Review and Peer Evaluation Meeting*; Washington, DC, United States, June 6−10, 2016, Project FC021, p 14.
(63) St-Pierre, J. *ACS Energy Lett.* in preparation.
(64) Freeman, B. D. Basis of Permeability/Selectivity Tradeoff Relations in Polymeric Gas Separation Membranes. *Macromolecules* **1999**, *32*, 375−380.
(65) Toni, E.; Minelli, M.; Sarti, G. C. A Predictive Model for the Permeability of Gas Mixtures in Glassy Polymers. *Fluid Phase Equilib.* **2018**, *455*, 54−62.
(66) St-Pierre, J. Hydrogen Mass Transport in Fuel Cell Gas Diffusion Electrodes. *Fuel Cells* **2011**, *11*, 263−273.
(67) Okada, T.; Ayato, Y.; Dale, J.; Yuasa, M.; Sekine, I.; Asbjørnsen, O. A. Oxygen Reduction Kinetics at Platinum Electrodes Covered with Perfluorinated Ionomer in the Presence of Impurity Cations Fe^{3+}, Ni^{2+} and Cu^{2+}. *Phys. Chem. Chem. Phys.* **2000**, *2*, 3255−3261.
(68) Okada, T.; Ayato, Y.; Satou, H.; Yuasa, M.; Sekine, I. The Effect of Impurity Cations on the Oxygen Reduction Kinetics at Platinum Electrodes Covered with Perfluorinated Ionomer. *J. Phys. Chem. B* **2001**, *105*, 6980−6986.
(69) Okada, T.; Satou, H.; Yuasa, M. Effects of Additives on Oxygen Reduction Kinetics at the Interface between Platinum and Perfluorinated Ionomer. *Langmuir* **2003**, *19*, 2325−2332.
(70) Qi, J.; Ge, J.; Uddin, M. A.; Zhai, Y.; Pasaogullari, U.; St-Pierre, J. Evaluation of Cathode Contamination with Ca^{2+} in Proton Exchange Membrane Fuel Cells. *Electrochim. Acta* **2018**, *259*, 510−516.
(71) Braaten, J. P.; Xu, X.; Cai, Y.; Kongkanand, A.; Litster, S. Contaminant Cation Effect on Oxygen Transport through the Ionomers of Polymer Electrolyte Membrane Fuel Cells. *J. Electrochem. Soc.* **2019**, *166*, F1337−F1343.
(72) St-Pierre, J. PEMFC Contamination Model: Neutral Species Sorption by Ionomer. *ECS Trans.* **2011**, *41*, 307−315.
(73) Weber, A. Z.; Kusoglu, A. Unexplained Transport Resistances for Low-Loaded Fuel-Cell Catalyst Layers. *J. Mater. Chem. A* **2014**, *2*, 17207−17211.
(74) Kongkanand, A.; Mathias, M. F. The Priority and Challenge of High-Power Performance of Low-Platinum Proton-Exchange Membrane Fuel Cells. *J. Phys. Chem. Lett.* **2016**, *7*, 1127−1137.

(75) Darling, R. Modeling Air Electrodes with Low Platinum Loading. *J. Electrochem. Soc.* **2019**, *166*, F3058−F3064.

https://dx.doi.org/10.1021/acs.jpcc.0c06233
J. Phys. Chem. C 2020, 124, 24052−24065